THE PENNSYLVANIA STATE UNIVERSITY
SCHREYER HONORS COLLEGE

DEPARTMENT OF MECHANICAL AND NUCLEAR ENGINEERING

EFFECT OF ELASTICITY ON LIQUID REPELLENCY OF CASSIE-STATE DROPLETS ON SUPERHYDROPHOBIC SURFACES

HANNAH FELDSTEIN
SPRING 2019

A thesis
submitted in partial fulfillment
of the requirements
for a baccalaureate degree
in Mechanical Engineering
with honors in Mechanical Engineering

Reviewed and approved* by the following:

Tak-Sing Wong
Assistant Professor of Mechanical Engineering and Biomedical Engineering
Thesis Supervisor

Hosam Fathy
Bryant Early Career Professor of Mechanical Engineering
Honors Adviser

* Signatures are on file in the Schreyer Honors College.

ABSTRACT

Many natural surfaces contain microstructures that are used to repel liquid. However, the effects of elasticity on liquid repellency have not been thoroughly investigated. A polydimethylsiloxane (PDMS) molding process was used to create microstructured superhydrophobic surfaces of varying elasticities and geometries. These surfaces were characterized using a sliding angle test in order to measure their liquid repellency. Overall, the results show that increasing the solid fraction results in poorer liquid repellency, for elasticities ranging from 1.18 MPa to 2.86 MPa. Additionally, some results suggest that increasing the Young's modulus of the micropillars also results in a higher degree of pinning due to a greater amount of energy consumed by pillar deformation.

TABLE OF CONTENTS

LIST OF FIGURES

LIST OF TABLES

ACKNOWLEDGEMENTS

I would like to thank various people for their help on this project. Firstly, I would like to express my deep appreciation for the excellent guidance of Dr. Tak-Sing Wong during this research experience. I also would like to thank Dr. Birgitt Boschitsch Stogin for being an incredible graduate student mentor. Additionally, I wish to thank everyone in the Wong Laboratory for Nature Inspired Engineering for creating a friendly and helpful lab environment. I would like to acknowledge Dr. Hosam Fathy for being an outstanding and supportive honors advisor through all of my endeavors at Penn State. Lastly, I want to thank my family and friends for making my undergraduate experience a great and memorable one.

Chapter 1

Introduction

In nature, we can find an infinite number of mechanisms, materials, and processes that inspire technological innovation. Water, being one of the most abundant liquids on our planet, is a thread that connects nearly all living things. Almost every plant or animal relies on water for its survival. As a result, we see numerous mechanisms in which life interacts with water. One of these mechanisms that is immensely useful in our everyday life is liquid repellency. Keeping liquid off of our surfaces has countless applications, ranging from something as simple as preventing fogging on eyeglasses to broader implementation such as water collection through means of fog and dew harvesting, or preventing friction on underwater vehicles.

Understanding the liquid repellency of a surface is critical for many applications. As indicated above, one major application is fog and dew harvesting. Water shortages are a major problem in many parts of the world, and finding an alternative source of clean water could greatly improve quality of life. Over two-thirds of the global population must live with water scarcity for at least one month of the year, and the demand for water only increases with a growing population. One possibility is to extract water out of air that contains water particles, such as fog or dew. By exposing a surface to fog or dew, water can be deposited onto the surface and then be removed for consumption.

In both fog and dew harvesting, there are three stages of water collection. The first stage involves water transport to the surface. The next stage is the capture of moisture onto the surface. This occurs more readily in fog harvesting than in dew harvesting, since water molecules

bombard the surface. The third and final stage is removal of water from the surface. This is an important step since it allows for greater water collection [1]. Through understanding the physics of various surface features, such as lubrication, elasticity, and nanoscale roughness, we can determine better ways to design surfaces for such applications.

Chapter 2

Literature Review

There are two main categories of superhydrophobic leaves. The first category consists of microstructures covering a leaf's surface. These microstructures often contain wax or hierarchical nanotextures to increase hydrophobicity. A primary example of this category is the lotus leaf. In this case, superhydrophobicity and liquid repellency are achieved because of small air pockets that are trapped underneath the droplet. Here, the liquid-air interface is increased, while the liquid-solid interface is decreased. The droplet consequently takes on a more spherical shape. The second category of superhydrophobic leaves are those covered in elastic hairs, which bend and suspend the droplet, preventing liquid from touching the main surface [2]. One example is a trichome, which may have a strong influence on wettability of leaf surfaces. Leaves with trichomes tend to be more liquid-repellent, especially with a higher trichome density [3]. Additionally, it was found that trichomes are a critical factor in determining the leaf's wettability. Surfaces with non-waxy trichomes can only repel water briefly after the water droplet makes contact with the surface, but wax-covered trichomes are consistently successful at liquid removal [4].

Wetting describes how well a liquid comes into contact with a solid surface, and is a critical factor in determining suitable applications. The degree of wetting relies on the ratio between energy necessary to extend the contact line and the energy required to increase the surface area of the liquid. The extent to which wetting occurs can be described by the contact angle, which is the angle between the horizontal surface and the tangent to the edge of the

droplet. Surfaces with a contact angle below 90º are considered to be hydrophilic, while surfaces with contact angles above 90º are hydrophobic. Additionally, superhydrophobic surfaces exhibit contact angles above 150º (indicating extremely unfavorable wetting), and superhydrophilic surfaces have contact angles of 10º or less. The contact angle on a smooth surface can be represented by Young's equation for surface wetting, and depends on the surface energies of the three different interfaces (solid-vapor, solid-liquid, and liquid-vapor):

$$\gamma_{SV} = \gamma_{SL} + \gamma_{LV}\cos(\theta), \qquad (1)$$

where γ_{SV} is the surface energy at the solid-vapor interface, γ_{SL} is the surface energy at the solid-liquid interface, γ_{LV} is the surface energy at the liquid-vapor interface, and θ is the contact angle of liquid on the smooth surface [5].

The degree of liquid repellency can be determined from the sliding angle, and the contact angle hysteresis. The sliding angle is the angle at which a surface must be tilted before the drop will begin to slide. It is critical that a sliding angle test is performed at very low tilting speeds in order to prevent momentum from causing the droplet to begin sliding before its true sliding angle. The contact angle hysteresis is the difference between the advancing and receding angles, which are the maximum and minimum angles, respectively, that a droplet exhibits while sliding on a surface. The advancing and receding angles can be determined by a number of methods. A commonly used method is the sliding angle test. The leading and lagging angles that a droplet exhibits once it begins to slide correspond to the advancing and receding angles respectively.

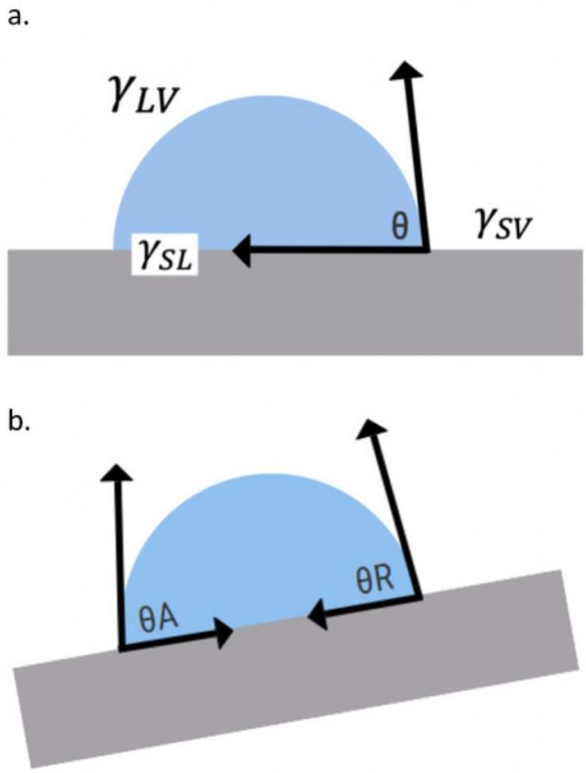

Figure 1. A visual representation of parameters used to characterize the hydrophobicity and liquid repellency of a surface: a) The apparent contact angle b) A sliding angle test, where θA is the advancing angle, θR is the receding angle, and θS is the sliding angle.

On surfaces that contain microstructures (such as those that we observe in nature), there are two common states in which a droplet can exist. The first state is the Cassie state, where the droplet is supported by the tops of the pillars and is therefore partially resting upon air. In this state, the droplet generally exhibits a high contact angle, and is easily repelled off of the surface. The second state occurs when the droplet is resting between the pillars, and is referred to as the Wenzel state. Here, strong pinning forces from the micropillars keep the droplet in place, trapping it on the surface. For surfaces that are meant to repel water, the Cassie state is highly favorable over the Wenzel state because it allows for a large apparent contact angle, and also

reduces the length of the liquid-solid interface (which therefore reduces the contact angle hysteresis) [6].

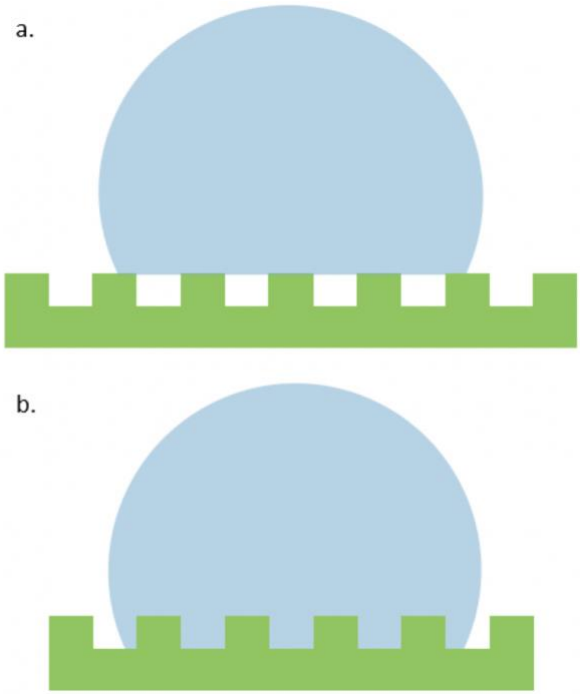

Figure 2. Schematics of a) a Cassie-state droplet on a rough surface, where the droplet is resting upon a combination of air and the tops of microstructures, and b) a Wenzel-state droplet that is resting in between the microstructures.

Micropillar geometry on a superhydrophobic surface has a profound effect on the contact angle of the surface. In the Cassie state, the contact angle can be described with the Cassie-Baxter equation:

$$\cos(\theta^*) = f_1 cos(\theta) - f_2 \qquad (2)$$

where θ^* is the predicted apparent contact angle of a Cassie-state droplet, f_1 is the fraction of solid underneath the droplet, and f_2 is the fraction of air underneath the droplet [7]. Therefore, the contact angle is inversely related with the solid fraction. Additionally, it is important to note that since Cassie-state droplets sit upon the tops of the microstructures, their contact angle is not

influenced by micropillar height. However, when droplets are in the Wenzel state, the height of the micropillars does have an influence on contact angle and liquid repellency. In order to represent the geometry of the entire micropillar, a roughness factor is used. Roughness can be defined as

$$r = 1 + \frac{4wh}{(w+l)^2}, \quad (3)$$

where w is micropillar width, l is the spacing between pillars, and h is the height of the micropillars. Qualitatively, the roughness factor is the ratio of the actual surface that the droplet makes contact with to the geometric surface. When a surface is perfectly smooth, the roughness factor is simply "1". The Wenzel equation represents how the contact angle on a smooth surface compares to the contact angle of a Wenzel-state droplet on a rough surface [8], which can be expressed as

$$cos\theta_W = r\ cos\ \theta, \quad (4)$$

where r is the roughness factor, θ_W is the apparent contact angle of a Wenzel-state droplet on a rough surface.

Additionally, the critical roughness for a droplet to transition from the Cassie state to the Wenzel state is given by

$$r_c = \Phi_{sf} - \frac{1-\Phi_{sf}}{\cos(\theta_{adv})}, \quad (5)$$

where r_c is the critical roughness at which a Cassie state droplet will transition into the Wenzel state, Φ_{sf} is the solid fraction, and θ_{adv} is the advancing contact angle [9].

Additionally, the micropillar geometry has a significant influence on liquid repellency, particularly for Cassie-state droplets. The effect of solid fraction on contact angle hysteresis of Cassie-state droplets, and the effect of roughness on contact angle hysteresis of Wenzel-state

droplets have been investigated. The solid fraction of a superhydrophobic surface is the fraction of the surface that is solid when a droplet is resting in the Cassie state. Solid fraction can be quantitatively defined as

$$\Phi_{sf} = \frac{w^2}{(w+l)^2} \qquad (6)$$

An increase in the solid fraction of a Cassie-state droplet results in a greater contact angle hysteresis. The contact angle hysteresis has long been hypothesized to be dependent upon the energy states at the three-phase contact point, i.e. at the edge of a droplet where liquid, air, and solid meet. Therefore, a possible explanation for this trend is that a lower solid-fraction surface requires less energy to expand the three-phase contact line. As a result, it is easier for a liquid to be repelled off of the surface. Wenzel-state droplets also displayed an increase in contact angle hysteresis as the surface roughness was increases. This may possibly be explained by the fact that a rougher surface requires more energy to expand the contact line because of increased area between the liquid and solid interface [10]. It is also important to note that the advancing angle and receding angle can be related to the sliding angle through

$$\frac{mgsin\theta_{slide}}{w_d} = \sigma(\cos\theta_{rec} - \cos\theta_{adv}), \qquad (7)$$

where m is the mass of the droplet, w_d is the droplet width, g is gravitational acceleration, σ is the surface tension, θ_{rec} is the receding angle, and θ_{slide} is the sliding angle [11].

Hair-covered surfaces are interesting because the hairs bend (absorbing elastic energy), and can therefore support the droplet above the surface. The Lady's Mantle, a plant covered in hydrophilic flexible hydrophilic hairs, exhibits hydrophobic properties. It should be noted that according to the Wenzel equation, a hydrophilic surface will become more hydrophilic with added roughness (the contact angle should decrease), and vice versa for a hydrophobic surface.

Therefore, it may initially seem perplexing that the Lady's Mantle is hydrophobic despite having hydrophilic hairs that provide a high degree of surface roughness. However, the reason that these surfaces are hydrophobic lies in the elasticity of the hairs. Extra energy is required in order to bend the hairs downward as the droplet wets the surface. This additional cost in energy prevents liquid droplets from penetrating the elastic hairs, thus allowing for a superhydrophobic surface. These hairy surfaces can be created synthetically using elastic materials such as a Poly (hydroxyethyl methacrylate) (PHEMA) network. However, it is important to note that the elasticity of hairs on the surface of the Lady's Mantle are 2.5 MPa, which is in the range of elasticity for materials such as PDMS.

Another important factor of hairy surfaces is whether the hairs will clump together, and if the water droplets will spread over the surface. Both of these effects are undesirable for fog or dew harvesting. In order to avoid clumping, hairs should be spaced a distance equal to at least half the length of the hairs. The critical droplet volume for spreading on a hairy surface is described by

$$V_s = \beta \left(\frac{\sigma d_s r_d L^3}{B(d_0 - d_s)}\right)^3, \qquad (8)$$

where β is a constant that is dependent upon droplet geometry, r_d is the radius of the droplet, d_0 is the diameter of the bottom of the hair, d_s is the diameter at the point of contact with the droplet, L is the hair length, and B is the bending stiffness [12].

There are three main factors that determine the energy of a droplet laying on top of elastic hairs. These are the wetting energy, capillary interaction, and energy absorbed in bending. The elastic energy required to deflect an elastic cylindrical "hair" a given distance is

$$E_{el} = \frac{3\pi E R^4}{8h^3} u^2, \qquad (9)$$

where E is the Young's modulus of the hair material, R is the hair radius, h is the height at which the hair contacts the droplet, and u is the deflection at a height of h on the hair. Wetting energy can be described by

$$E_{wet} = 2\pi Rh\sigma\cos(\theta_{cyl}), \quad (10)$$

where θ_{cyl} is the contact angle of the fluid interface with the hair. For capillary lengths of q^{-1} or smaller, a logarithmic curve can represent capillary action forces (where $q = [\sigma/(\rho g)]^{1/2}$ represents the inverse capillary length, where ρ is the water density). Once the capillary length exceeds q^{-1}, the capillary force decays exponentially [13].

PDMS is one of the most commonly used silicone-based organic polymers, and can be used in order to create elastic superhydrophobic surfaces. Additionally, it is generally inert, nontoxic, and inexpensive, making it a popular material for a variety of applications. The elasticity of PDMS can be varied by altering the degree to which the polymer network is allowed to crosslink. A higher degree of crosslinking results in a more rigid surface. PDMS is composed of two main chemicals: the base and the curing agent. In order to tune the amount of crosslinking, the ratio of PDMS base to PDMS curing agent is altered. An increased curing agent ratio will result in a higher degree of crosslinking, and therefore a more rigid surface. A PDMS curing agent ratio ranging from 5:1 to 33:1 can result in elastic moduli ranging from 0.75 to 3.7 MPa [12]. It should be noted that PDMS micropillars may collapse once the aspect ratio of height to base width exceeds 10 [10]. An inverse relationship exists between the Young's modulus and the ratio of base to curing agent, which is expressed by

$$E = \frac{20\ MPa}{n} \quad (11)$$

Here, n is the ratio of curing agent to PDMS base. This equation was found empirically by fitting a curve to measured tension and compression stiffness values. The addition of a curing agent will continue to stiffen the PDMS until a base to curing agent ratio of 5:1 is reached [14].

Chapter 3

Materials and Methods

A simple PDMS molding system was used in order to create elastic slippery rough surfaces. The elasticity was varied by altering the ratio of PDMS base to curing agent. Additionally, a total of eight pillar geometries were fabricated and tested. The liquid-repellency was determined through a series of tilting angle tests. Both the sliding angle and contact angle hysteresis were used for characterization.

Sample Fabrication

Elastic samples were created from a silanized superhydrophobic silicon wafer containing micropillars (fabricated by PhD student, Nan Sun). A mold was made of PDMS with a base and curing agent ratio of 1:10, mixed by hand for five minutes, and set in the ARE-310 centrifugal mixer at 2000 revolutions per minute for 30 seconds, and 2200 revolutions per minute for another 30 seconds. Next, the sample was poured onto the microtextured silicon wafer and placed in a vacuum for 15 minutes in order to release air bubbles. Excess bubbles were removed with a pipette. The sample was then allowed to crosslink for 48 hours before the mold was removed from the silicon wafer. Next, this PDMS mold was silanized with 1H, 1H, 2H, 2H-Perfluorodecyltrichlorosilane, 96% for 24 hours to allow for separation between the PDMS mold and the final PDMS superhydrophobic surface sample.

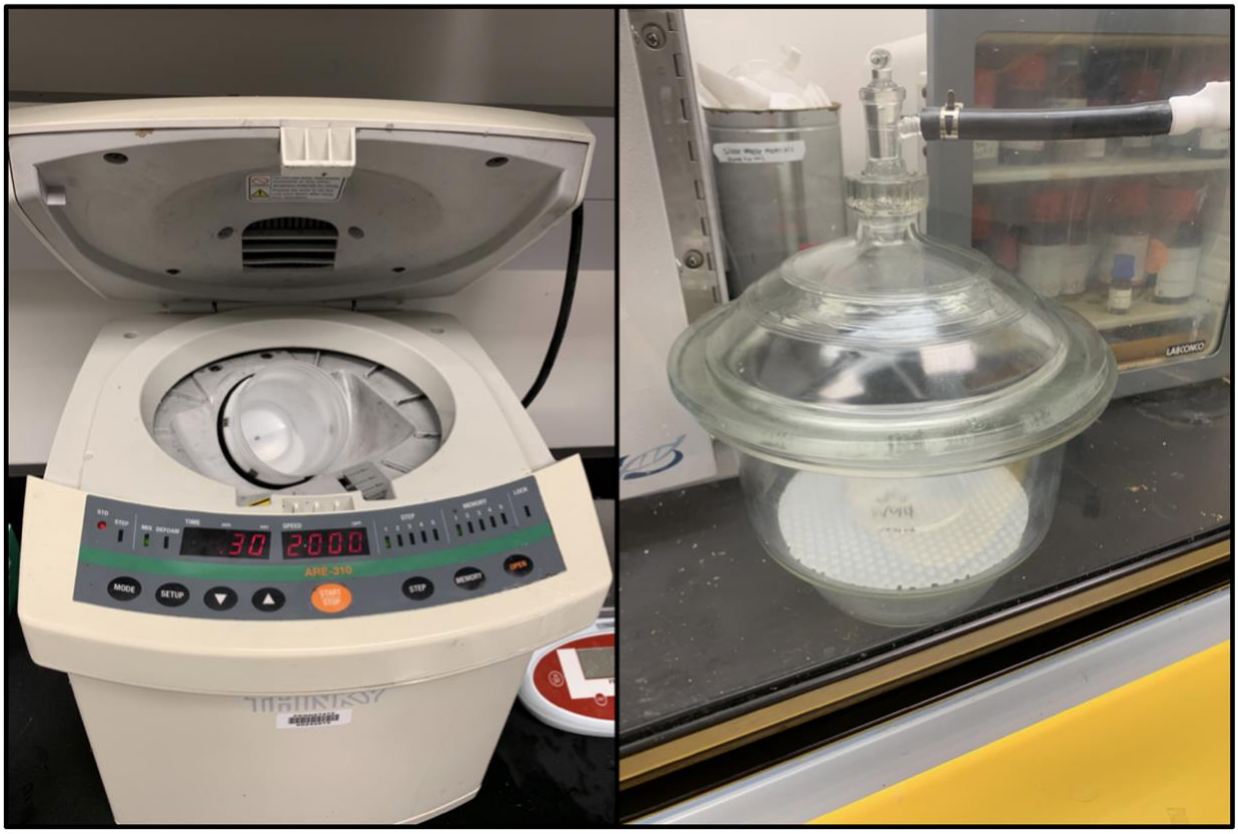

Figure 3. The two major processes used to remove bubbles from the surface were spinning the liquid PDMS in a centrifuge (left) and placing the mold and PDMS inside of a vacuum (right).

Seven PDMS samples were fabricated, each with a different elasticity. The elasticity was varied by altering the curing agent to base ratio (1:7, 1:9, 1:10, 1:12, 1:14, 1:15, and 1:17). Each liquid PDMS sample was placed in the ARE-310 centrifugal mixer for 30 seconds at 2000 revolutions per minute, and for 30 seconds at 2200 revolutions per minute. Each sample was then poured over the silanized PDMS mold, and placed in a vacuum for 15 minutes to promote the release of air bubbles. Excess bubbles were removed by pipet.

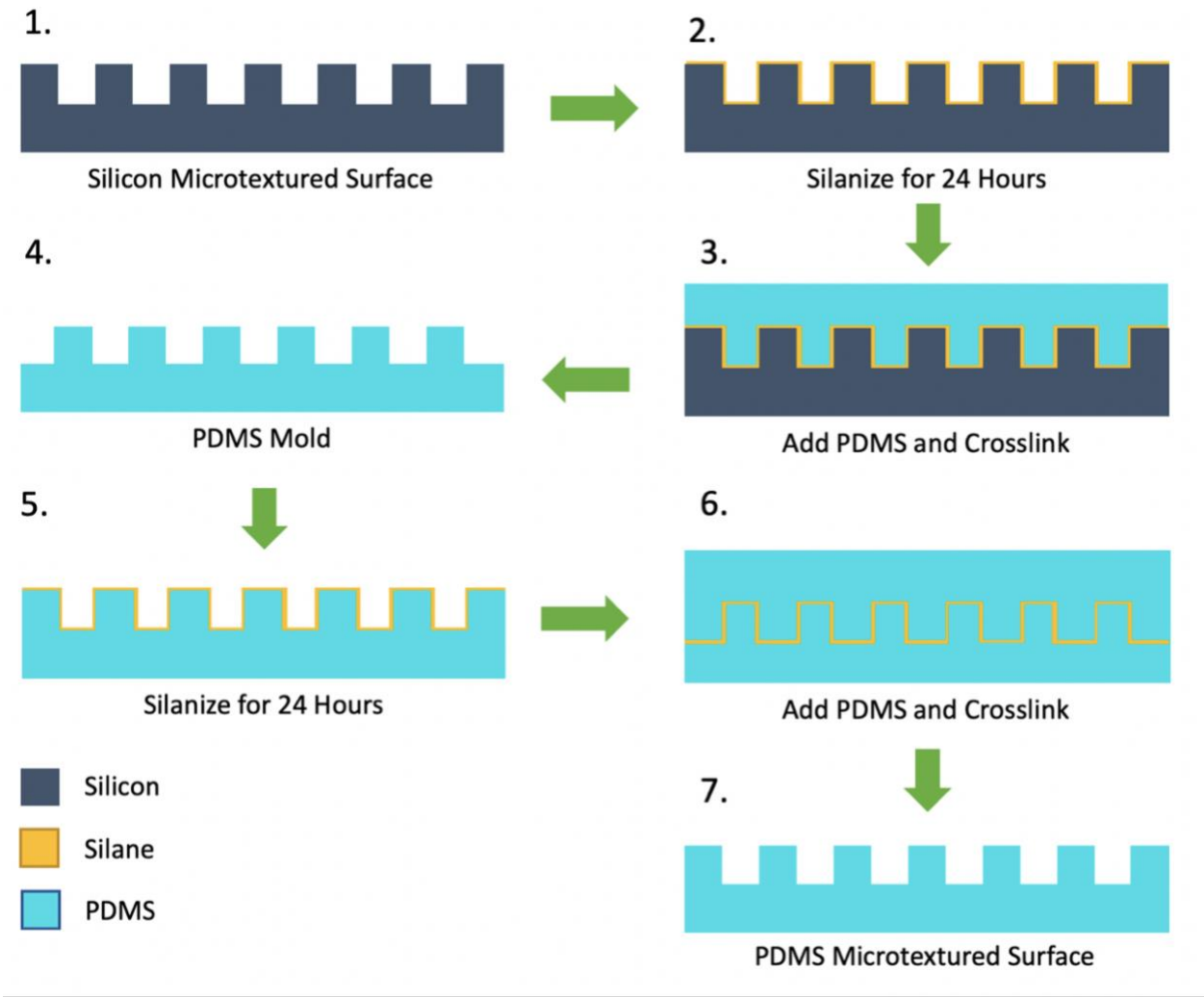

Figure 4. A schematic of the PDMS superhydrophobic manufacturing process shows the six stages used to create an elastic superhydrophobic surface.

The sample was then placed in an oven at 60ºC for 3 hours and 30 minutes to promote crosslinking. The samples were separated from the PDMS mold, which was reused for the remaining PDMS samples.

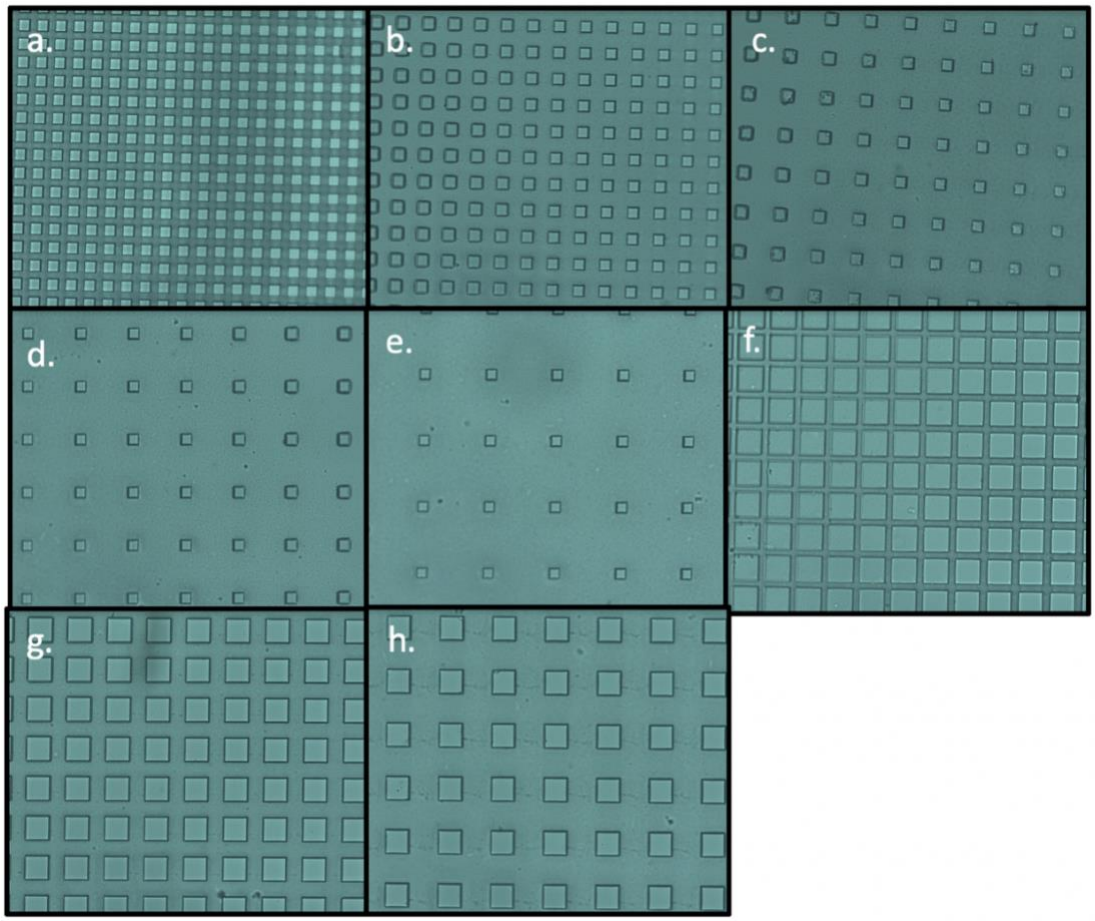

Figure 5. Microscopic images of PDMS superhydrophobic surface samples with a PDMS base to curing agent ratio of 1:10, at 20x magnification, for geometries of a) 25 µm width, 10 µm spacing, and 100 µm height b) 25 µm width, 25 µm spacing, and 100 µm height c) 25 µm width, 50 µm spacing, and 100 µm height d) 25 µm width, 75 µm spacing, and 100 µm height e) 25 µm width, 100 µm spacing, and 100 µm height f) 50 µm width, 10 µm spacing, and 100 µm height g) 50 µm width, 25 µm spacing, and 100 µm height h) 50 µm width, 50 µm spacing, and 100 µm height micropillars.

Goniometer Testing

The liquid-repellencies of the elastic superhydrophobic surfaces were determined through a series of tilting angle tests performed with a goniometer (ramé-hart Model 295). The sample

was cleaned with distilled water and dried with nitrogen gas in order to help remove any excess dust particles from the surface. The goniometer was initialized with 10 cycles in the “Drop Volume Control” menu and a sphere calibration was measured. Next, the sample was placed on the goniometer and adjusted until the surface was completely flat using the “Baseline Setup” feature. A 25 mL droplet of distilled water was placed on the flat surface. A new “Contact Angle” experiment was created with tilt, and set to 250 measurements, measured every 0.5 seconds, starting from 0º to 90º. The base was tilted at an average rotational speed of 0.72 degrees per second, with a photo taken every approximately every 2 seconds, or every 0.36 degrees.

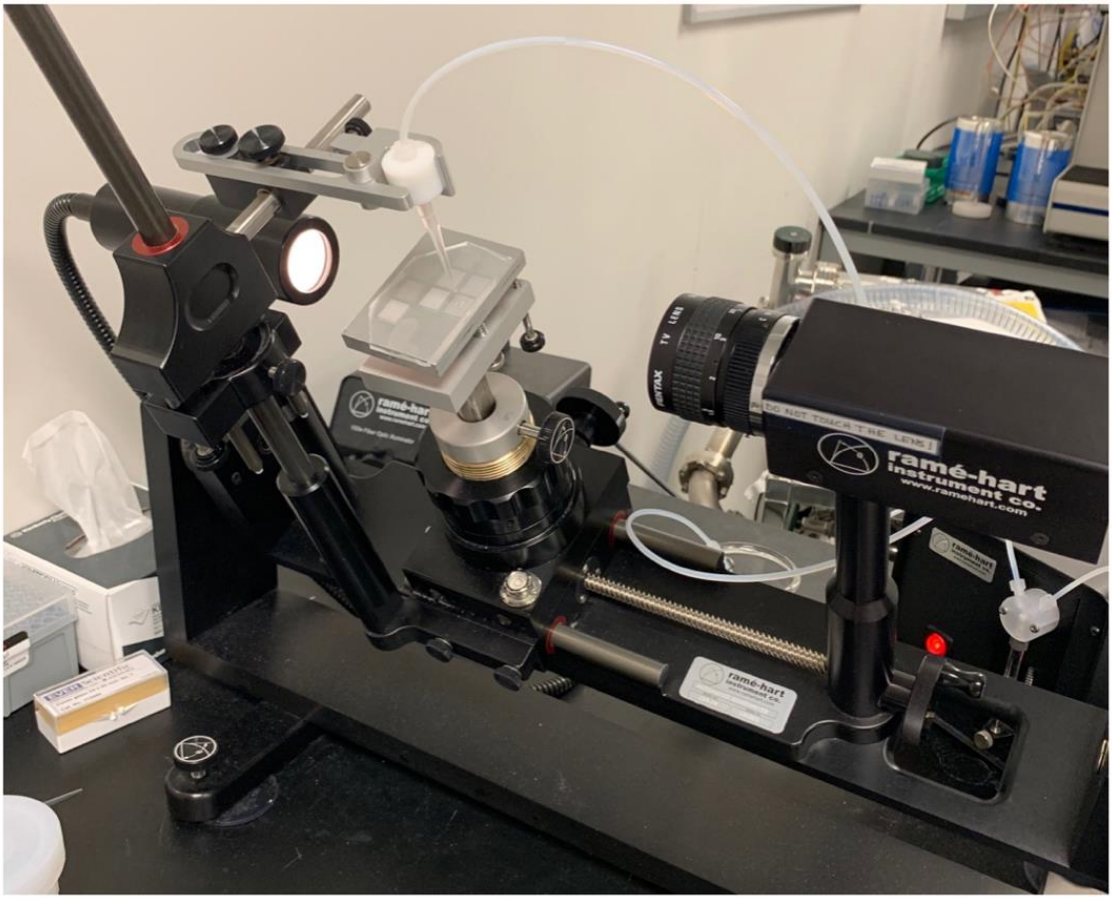

Figure 6. The goniometer setup used for the sliding angle test is shown.

Image Analysis

The sliding angle was recorded as the angle at which the droplet first begins to slide. Next, the “drop_analysis” plugin with the “DropSnake” feature in ImageJ was used to analyze the advancing and receding angles on an image of the droplet just as sliding began.

In the Contact Angle plugin, one point was placed at each of the two three-phase contact points. Five additional points were added to the liquid-air interface of the droplet. Next, a

"Manual Points Procedure" was run in order to determine the contact angle of the right and left sides of the droplet. Left and right contact angle data from the elliptical analysis was used.

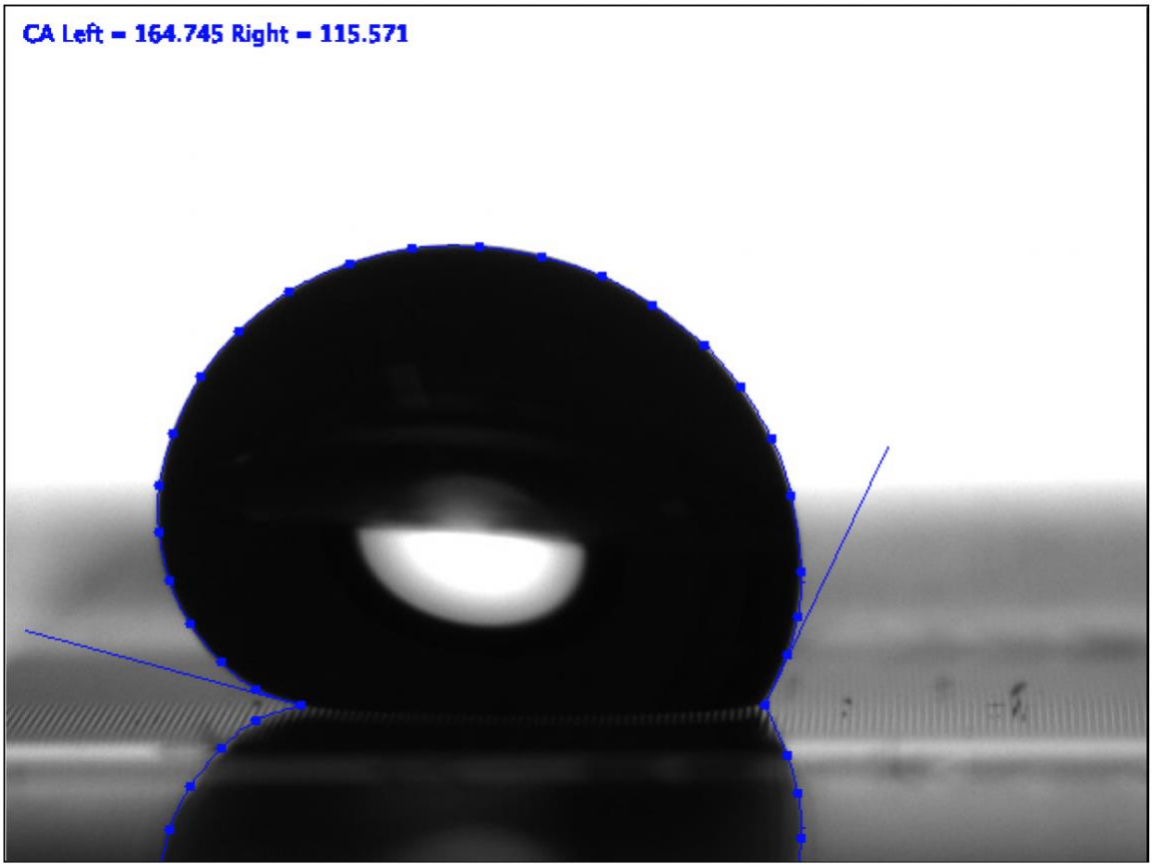

Figure 7. ImageJ Drop Analysis - DropSnake method used to determine advancing and receding angles on the 25 µm width, 25 µm spacing, and 100 µm height microstructures made with a PDMS curing agent to base ratio of 1:7.

The Young's modulus of each of the seven surfaces was determined using Eq. 10. The resulting Young's moduli for the surfaces were 2.86 MPa, 2.22 MPa, 2.00 MPa, 1.67 MPa, 1.43

MPa, 1.33 MPa, and 1.18 MPa. The specific amounts of PDMS base and curing agent used to fabricate each surface are indicated in Table 1.

Table 1. Weights of PDMS base and curing agent

	1:7 Ratio Surface	***1:9 Ratio Surface***	***1:10 Ratio Surface***	***1:12 Ratio Surface***	***1:14 Ratio Surface***	***1:15 Ratio Surface***	***1:17 Ratio Surface***
PDMS Base (g)	19.72	20.26	23.97	20.02	23.19	23.34	22.72
Curing Agent (g)	2.84	2.42	2.38	1.66	1.64	1.57	1.35

Surface Energy Comparison of PDMS

Before testing the elastic microtextured surfaces of various PDMS base to curing agent compositions, it was important to verify that these different ratios would not have any significant influence on the PDMS surface chemistry (and surface energy). In order to test for this property,

contact angle measurements were taken on flat PDMS surfaces of each of the seven compositions (see Fig. 8).

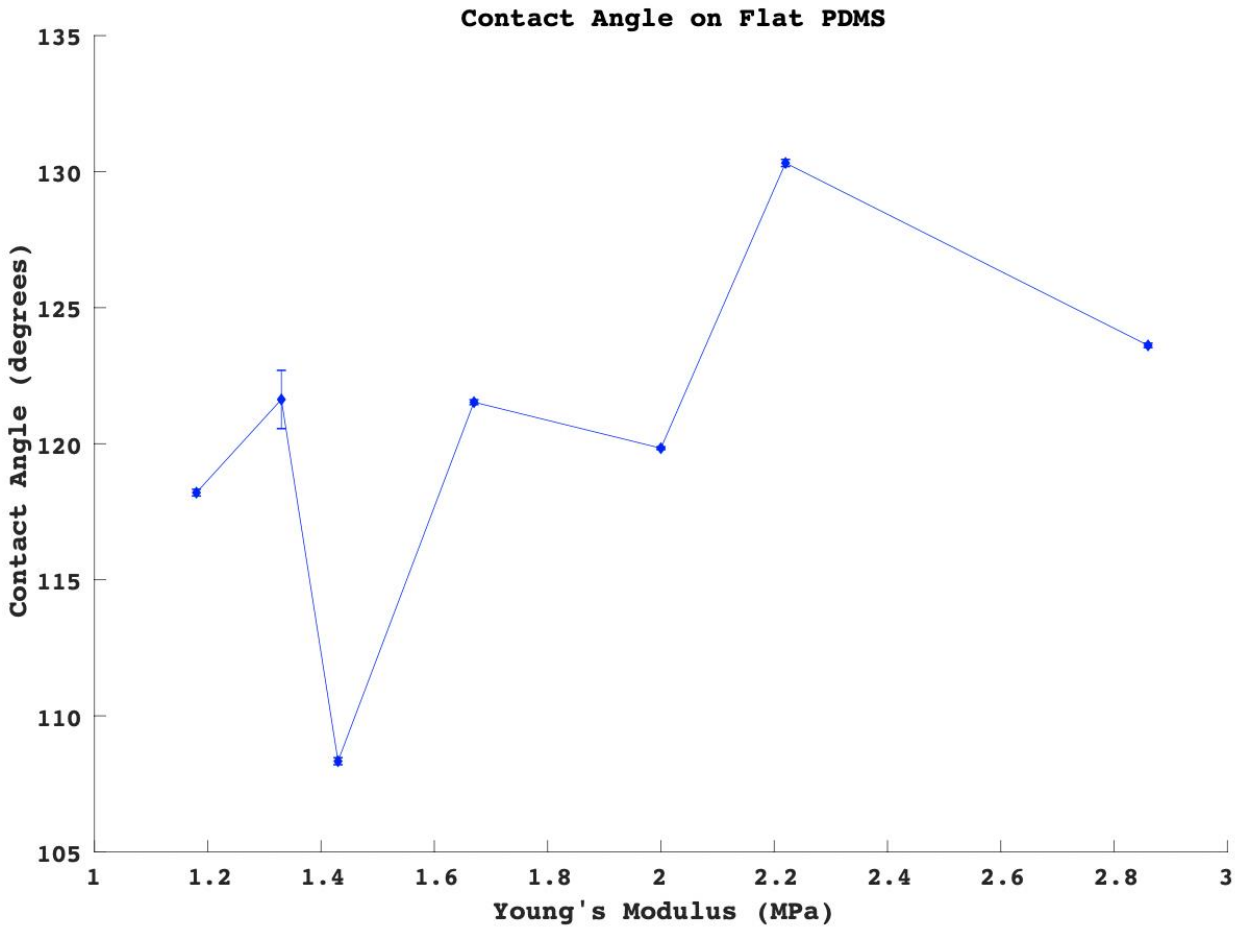

Figure 8. Contact angle on flat PDMS surfaces of various base to curing agent ratio compositions.

From these results, we can see that there does not appear to be any significant correlation between the contact angle and Young's Modulus.

Chapter 4

Results and Discussion

Sliding angle tests were performed on the seven microtextured superhydrophobic surfaces with varying elasticity. Both the sliding angle and contact angle hysteresis were analyzed to determine the effect of elasticity on liquid repellency of superhydrophobic surfaces.

Verification of Pillar Bending

Before testing, an important step was to show that the micropillars were indeed capable of bending from surface tension forces of a water droplet. In order to demonstrate this capability, a water droplet was placed on the 1.18 MPa surface, and pillar bending was observed as the droplet evaporated.

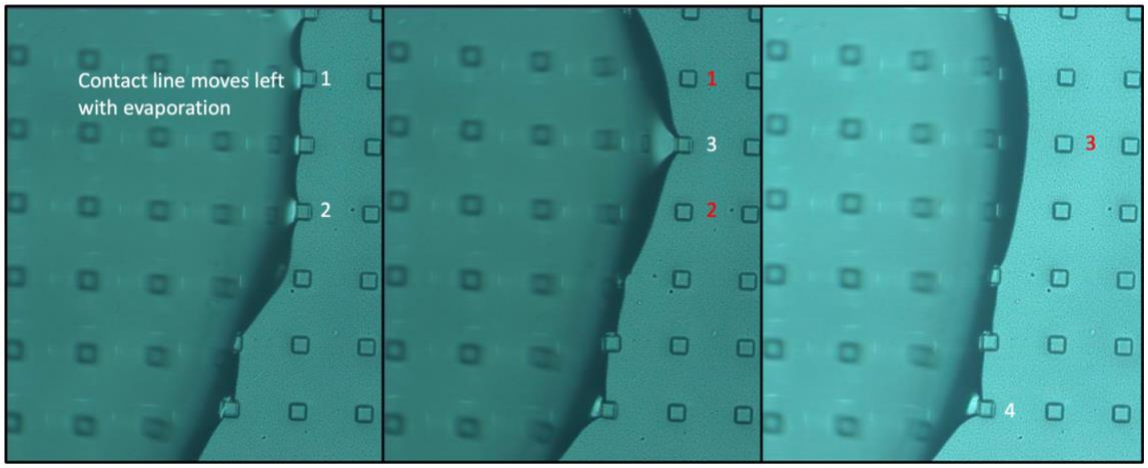

Figure 9. Bending can be observed in individual pillars (on the 1.18 MPa surface) before the contact line is released. Pillars on the verge of snapping are labeled in white, while pillars that have been released from the left-moving contact line are indicated in white.

In Fig. 9, subtle bending can be observed on pillars right before they are released from the contact line. As the droplet evaporates, the contact line shifts towards the left, pulling the pinned micropillars in this direction. The bending effect is mainly visible in pillars that are being stretched by surface tension from the contact line. From a bird's-eye view, micropillar bending is visible in these pillars because the top of the pillar shifts towards the contact line, and the sides of the pillars are partially visible. Once a micropillar is released from the contact line, it reverts back to its original position, and its sides are no longer visible. On our most elastic surface (1.18 MPa), we only observe a very slight bending. This hints that while we may observe some changes in sliding angle and contact angle hysteresis as a function of bending, this variation may be very subtle.

Sliding Angle

The sliding angle was measured on the goniometer, and was plotted both as a function of solid fraction and as a function of elasticity. Previous studies have shown that the contact angle hysteresis increases with solid fraction [11]. Additionally, an increased contact angle hysteresis is correlated with a greater sliding angle [10]. It is important to note that this trend extends to elastic surfaces as well, with all seven surfaces of various elasticity all showing a clear trend of increasing sliding angle as a function of solid fraction (See Fig. 10).

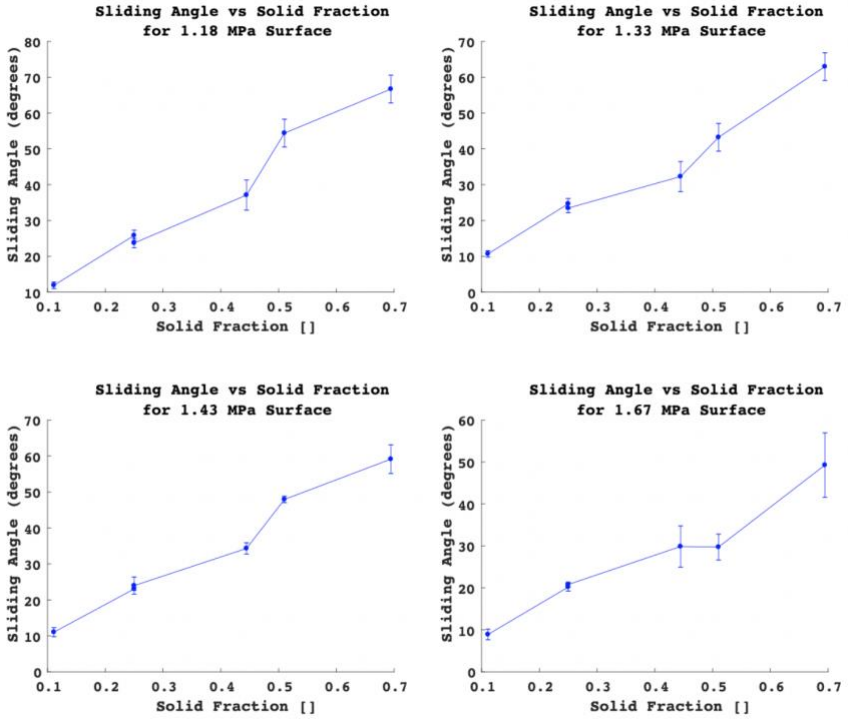

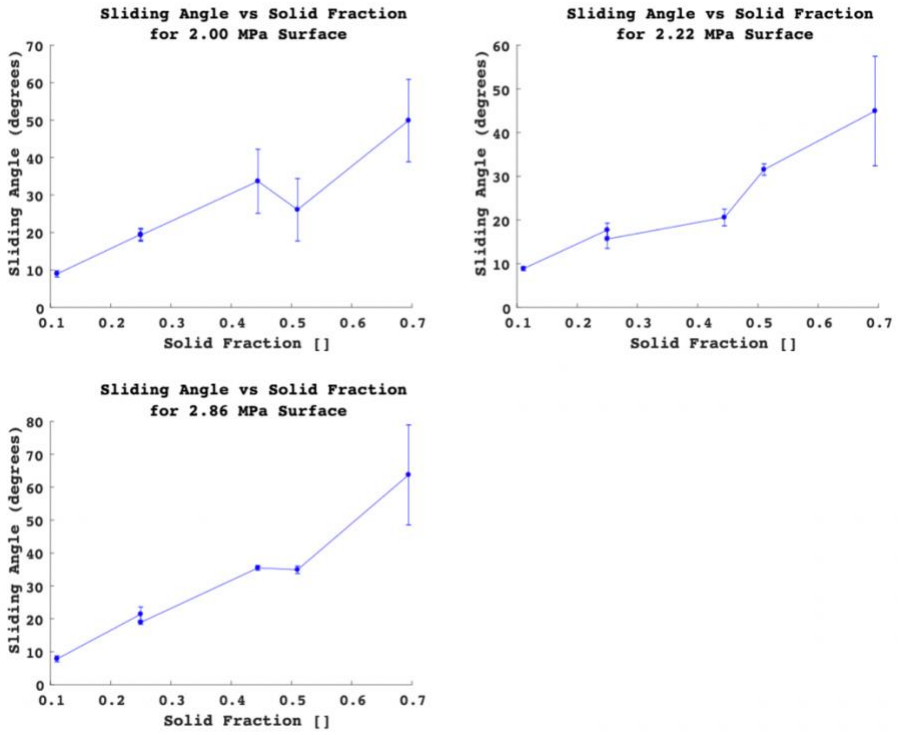

Figure 10. Sliding angle is shown as a function of solid fraction for varying elasticities, where error bars represent one standard deviation.

We also examined how varying the elasticity influenced the sliding angle of the droplet (see Fig. 11). This is a relatively weak correlation, although an overall downward trend may exist.

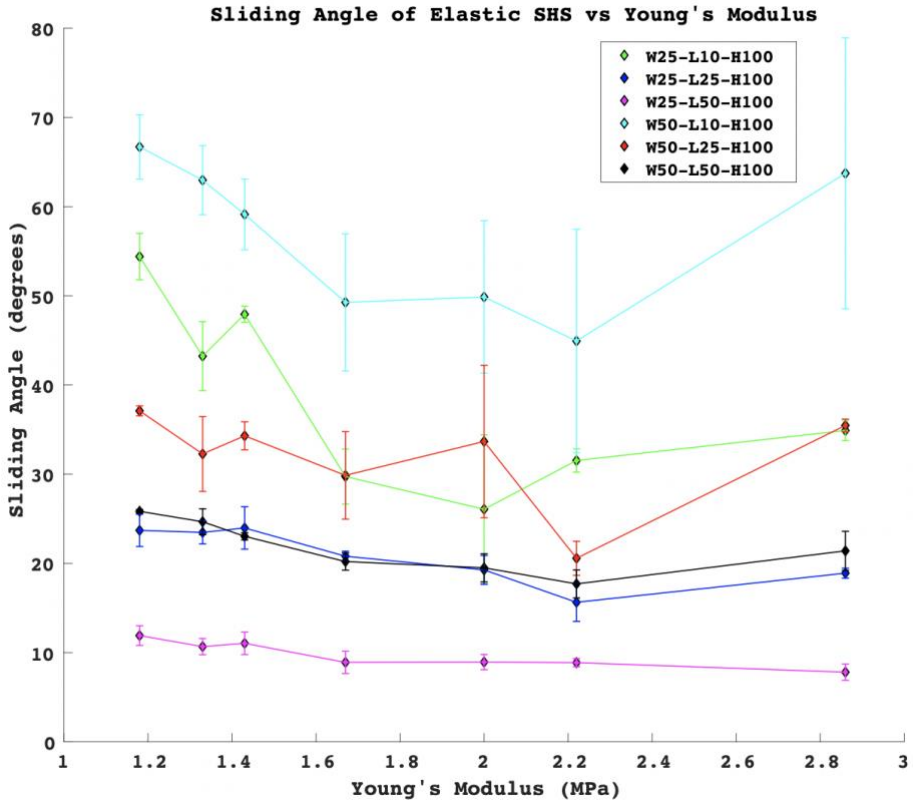

Figure 11. Sliding angle is shown as a function of elasticity. Error bars represent one standard deviation. Additionally, 'W' refers to the micropillar width, 'L' corresponds to the spacing between the micropillars, and 'H' represents the height of the micropillars. These values are given in microns.

It is also important to note that some of the sliding angles contain very large errors. This is particularly true for the larger sliding angles. This may be attributed to the fact that especially at a higher roughness, the water droplets became somewhat unstable, possibly due to the elastic nature of PDMS, as droplets in the Cassie state could sometimes fall into a transition phase. Here, part of the droplet remained in the Cassie state while another section of the same droplet penetrated the surface and rested in between the microstructures, contributing to extra droplet pinning. As a result, we observe a relatively high standard deviation in the sliding angles of some of these surfaces. It is also notable that we observe a slight increase in the sliding angle at 2.86

MPa (the highest Young's modulus). Whether this is indicative of an optimal stiffness to minimize the sliding angle is something that can be further investigated. See Appendix A for sliding angle values.

Contact Angle Hysteresis

The contact angle hysteresis was also measured, and plotted as a function of solid fraction (see Fig. 12). Once again, we can observe a direct relationship between contact angle hysteresis and solid fraction of the surface. The standard deviation is notably higher in the contact angle hysteresis data than in the sliding angle data. This also may be partially attributed to the instability of droplets in the Cassie state on elastic superhydrophobic surfaces. See Appendix B for values of the contact angle hysteresis, and advancing and receding angles.

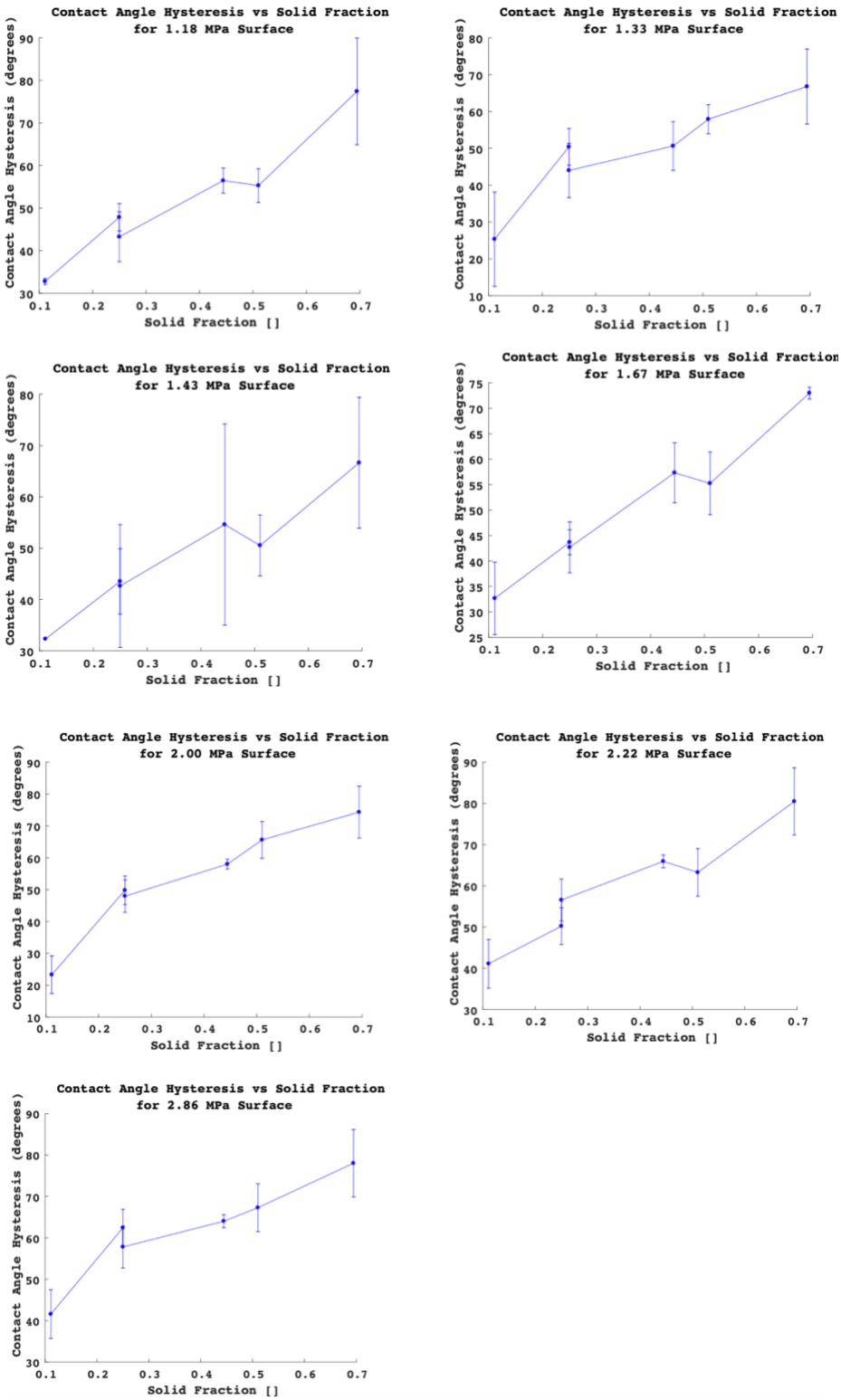

Figure 12. Contact angle hysteresis is shown as a function of solid fraction for varying elasticities, where error bars represent one standard deviation.

The effects of elasticity on contact angle hysteresis were also examined. Once again, we observe a possible slight downward trend in the contact angle hysteresis as the elasticity increases. Additionally, it appears that the contact angle hysteresis may level off at some point past approximately 1.6 MPa. Once a certain stiffness is achieved, the effects of bending on contact angle hysteresis may become negligible (see Fig. 13).

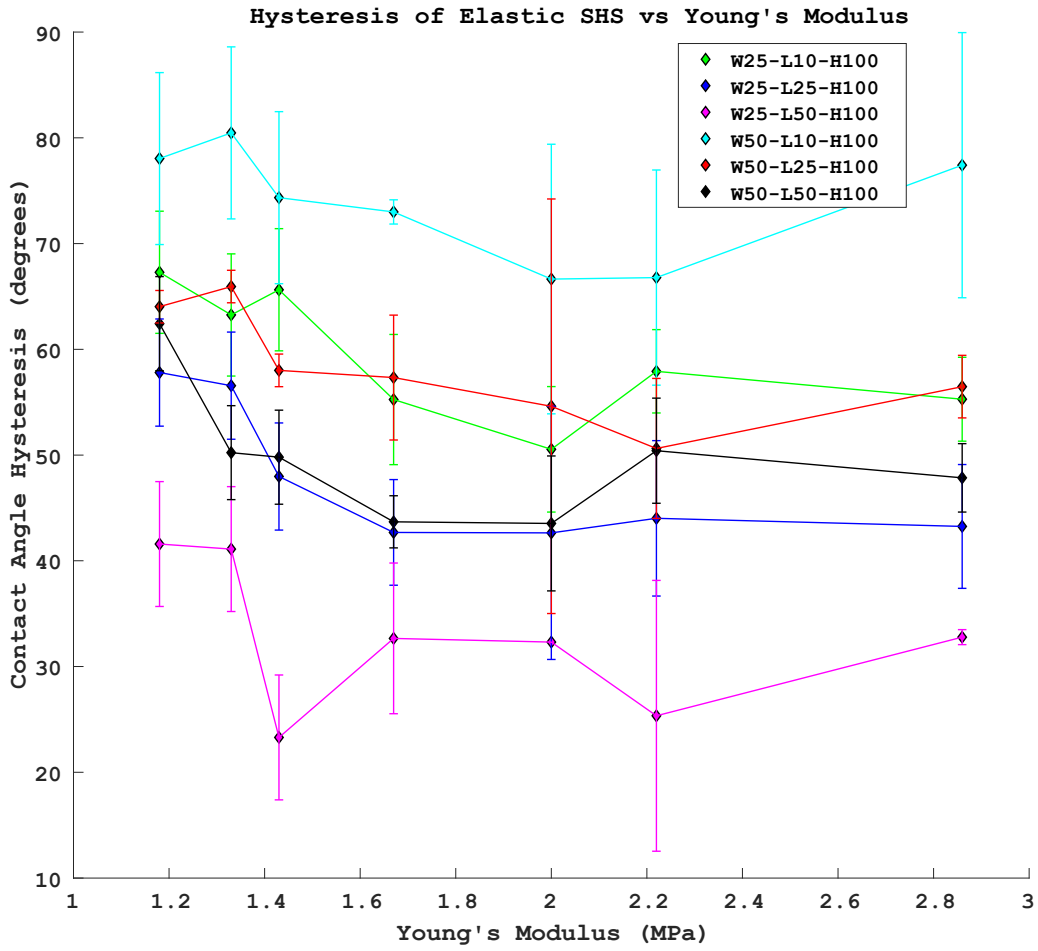

Figure 13. Contact angle hysteresis is shown as a function of elasticity. Error bars represent one standard deviation. Additionally, 'W' refers to the micropillar width, 'L' corresponds to the spacing between the micropillars, and 'H' represents the height of the micropillars. These values are given in microns.

Energy Analysis

The mechanisms behind the effect of solid fraction on liquid repellency of Cassie-state droplets (sliding angle and contact angle hysteresis) on rigid surfaces has already been established [11]. However, it is important to explore the physics of how elastic pillars may tend to have poorer liquid repellency.

On a tilted surface, the work that a droplet does can be represented by

$$W = mgsin(\alpha)dl, \tag{12}$$

where W is the work done by the droplet, α is the sliding angle, and dl is the distance descended by the drop. The downward force produced by the droplet is simply $mgsin(\alpha)$ [10].

For a droplet to slide on a rigid surface, this force must exceed the pinning force that is caused by roughness on the surface (e.g. micropillars). However once elasticity is added into the equation, we gain another energy factor. As established by Eq. 9, energy is lost by deforming the flexible pillars [13]. Each micropillar is effectively a cantilever beam. When a droplet is pinned to a micropillar, additional energy may be consumed by the droplet's downward force term ($mgsin(\alpha)$) towards bending the micropillars.

Since these droplets are in the Cassie state, they only interact with the tops of the micropillars.. Therefore, we can assume that the force acts on the ends of each pillar. The deflection of an end-loaded cantilever beam is represented as:

$$\delta_x = \frac{FL^3}{3EI} \tag{13}$$

where δ_x is the end-of-beam deflection in the direction that the force is applied, F is the end-loaded force, L is the length of the cantilever (equivalent to micropillar height in this scenario), E is the Young's Modulus, and I is the area moment of inertia. It is important to note that this

system is not truly a horizontally deflected end-loaded cantilever beam, because a droplet resting on the surface contains both a horizontal force due to droplet surface tension (contributing to horizontal deflection), and a downward force that contributes to buckling.

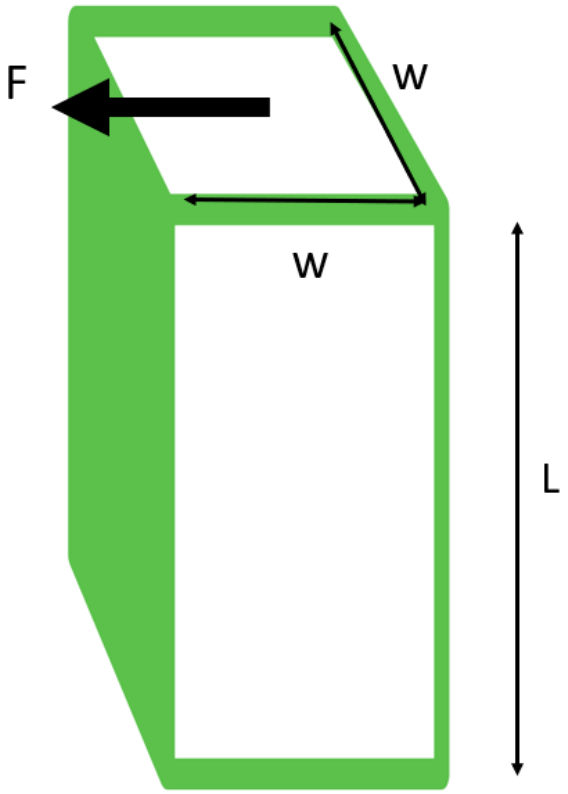

Figure 14. A schematic of the distances and approximations used in assessing the micropillars as cantilever beams.

Here, the area moment of inertia (I) is defined as:

$$I = \frac{w^4}{12} \qquad (14)$$

The $\frac{3EI}{L^3}$ term in Eq. 13 is essentially a stiffness term, since Eq. 13 can be written as $F = (\frac{3EI}{L^3})\delta_x$. This stiffness term can be changed in only two ways, since for our experiments, L (height of the micropillars) is fixed at 100 μm. The first way in which we can alter this stiffness

term is by changing the area moment of inertia. This can be achieved by tuning the width of the pillars (w), which the area moment of inertia is highly sensitive to, as width is multiplied to the fourth power. The second manner in which we can increase the stiffness term is by increasing the Young's modulus. This was accomplished by fabricating PDMS with a low ratio of base to curing agent. However, this analysis shows that if we analyze the deflection in elastic micropillars from an end-loaded cantilever approach, the width of the micropillars is significantly more important than the Young's modulus. In our experiments, the width was varied between 25 μm and 50 μm. The Young's modulus was varied from 1.18 MPa to 2.86 MPa. From Eq. 13 and Eq. 14, we can see that by doubling the width of a micropillar, the stiffness term will increase by a factor of 16. However, when doubling the Young's modulus, the stiffness term only increases by a factor of 2. This indicates that the stiffness is much more sensitive to changes in micropillar width than to changes in Young's modulus. Additionally, altering the length of the micropillars would have a strong influence on the stiffness term, as length is multiplied to the negative third power. Young's modulus has a significantly weaker effect on the overall stiffness term than the geometric parameters (width and height). Therefore, it makes sense that we do not see a dramatic change in the resulting sliding angles and contact angle hysteresis with changing Young's modulus.

Chapter 5

Conclusions and Future Work

Sliding angle tests have shown that changing the geometry and Young's modulus of micropillars on superhydrophobic surfaces can have a profound influence on the liquid repellency properties. Namely, for rigid superhydrophobic surfaces containing microstructures, the direct relationship between solid fraction and contact angle hysteresis and sliding angle in Cassie-state droplets has already been established. However, these results show that this still holds true for microtextured surfaces with elasticities as low as 1.18 MPa. Additionally, we observe a slight overall increase in the sliding angle and contact angle hysteresis with higher flexibility. This relationship should be further investigated for precise characterization.

There are many more avenues in which this work can be extended. Firstly, it would be useful to continue studying Cassie-state droplets on elastic surfaces, but varying the geometry and elasticity to a greater extent. A potential challenge in further decreasing the Young's modulus of PDMS is that once a base to curing agent ratio of approximately 20:1 is achieved, it becomes more difficult to consistently manufacture pillars without any breakage. However, infinite geometries exist that can be used to change the overall micropillar stiffness. It would also be interesting to see how altering the elasticity and geometry influences liquid repellency of droplets in the Wenzel state.

Another potential path to explore is the addition of lubricant to the PDMS surfaces. Lubricant can greatly reduce pinning, resulting in a much more liquid-repellent surface. It would be interesting to explore whether stiffness still has an increased pinning effect even when the

micropillar pinning is minimal. One challenge with addressing this question is how to manufacture a PDMS surface with a thin, robust lubricant coating.

Appendix A

Sliding Angle Data

Table 2. Sliding angle values for each tested surface

	25W 10L 100H (μm)	**25W 25L 100H (μm)**	**25W 50L 100H (μm)**	**50W 10L 100H (μm)**	**50W 25L 100H (μm)**	**50W 50L 100H (μm)**
1.18 MPa	52.7 º	22.0 º	13.0 º	63.2 º	37.2 º	26.0 º
	57.4 º	23.5 º	10.8 º	70.4 º	37.6 º	25.6 º
	53.1 º	25.6 º	11.9 º	66.5 º	36.5 º	25.9 º
1.33 MPa	40.8 º	23.1 º	10.8 º	58.5 º	27.5 º	26.3 º
	47.7 º	24.9 º	9.7 º	65.4 º	33.9 º	23.5 º
	41.2 º	22.4 º	11.5 º	65.0 º	35.4 º	24.2 º
1.43 MPa	47.0 º	22.4 º	12.2 º	56.0 º	33.6 º	22.8 º
	48.8 º	26.7 º	9.7 º	57.8 º	36.1 º	23.5 º
	48.0 º	22.8 º	11.2 º	63.6 º	33.2 º	22.8 º
1.67 MPa	26.4 º	20.2 º	10.1 º	53.5 º	24.2 º	21.3 º
	32.5 º	21.3 º	9.0 º	53.9 º	32.5 º	19.5 º
	30.3 º	20.9 º	7.6 º	40.4 º	32.9 º	19.8 º
2.00 MPa	21.3 º	20.2 º	9.9 º	37.2 º	23.8 º	20.6 º
	21.2 º	17.4 º	8.6 º	57.1 º	38.6 º	20.6 º
	35.7 º	20.2 º	8.3 º	55.3 º	38.6 º	17.7 º

2.22 MPa	31.4 º	14.4 º	9.4 º	58.9 º	18.4 º	18.4 º
	30.3 º	14.4 º	8.6 º	34.7 º	22.0 º	15.9 º
	32.9 º	18.1 º	8.6 º	41.2 º	21.3 º	18.8 º
2.86 MPa	33.6 º	19.5 º	6.8 º	79.5 º	35.6 º	23.8 º
	35.4 º	18.4 º	8.6 º	62.5 º	36.1 º	20.9 º
	35.7 º	18.8 º	8.0 º	49.2 º	34.7 º	19.5 º

Appendix B

Contact Angle Hysteresis Data

Table 3. Advancing and receding angle data for 25W 10L 100H (µm) and 25W 25L 100H (µm)

	25W 10L 100H (µm)			***25W 25L 100H (µm)***		
	Adv. Angle (º)	Rec. Angle (º)	Hysteresis (º)	Adv. Angle (º)	Rec. Angle (º)	Hysteresis (º)
1.18 MPa	155.422	85.385	70.037	164.576	108.541	56.035
	153.54	82.301	71.239	166.808	111.883	54.925
	149.924	89.349	60.575	172.050	109.603	62.447
1.33 MPa	155.536	95.962	59.574	162.861	107.482	55.379
	153.304	86.081	67.223	168.725	108.183	60.542
	149.738	86.781	62.957	162.334	108.573	53.761
1.43 MPa	148.011	82.790	65.221	158.722	107.291	51.431
	155.445	83.683	71.600	153.338	111.182	42.156
	151.445	91.376	60.069	162.252	111.919	50.333
1.67 MPa	147.852	99.708	48.144	158.145	113.193	44.952
	148.231	89.136	59.095	158.66	121.702	36.958
	156.387	97.886	58.501	155.654	109.506	46.148
2.00 MPa	162.633	110.984	51.649	158.866	127.788	29.078

	151.567	107.435	44.132	162.930	111.214	51.716
	163.759	107.917	55.842	157.566	110.432	47.134
2.22 MPa	155.871	97.970	57.901	166.5	117.101	49.399
	152.034	98.047	53.987	161.806	114.799	47.007
	155.976	94.105	61.871	153.543	117.902	35.641
2.86 MPa	150.461	99.036	51.425	164.745	115.571	49.174
	149.723	94.644	55.079	154.651	117.182	37.469
	155.595	96.246	59.349	161.991	118.873	43.118

Table 4. Advancing and receding angle data for 25W 50L 100H (μm) and 50W 10L 100H (μm)

	25W 50L 100H (μm)			***50W 10L 100H (μm)***		
	Adv. Angle (º)	Rec. Angle (º)	Hysteresis (º)	Adv. Angle (º)	Rec. Angle (º)	Hysteresis (º)
1.18 MPa	174.334	121.908	52.436	141.176	72.786	68.390
	168.743	129.763	38.980	160.747	72.580	88.167
	161.21	127.872	33.338	155.852	78.295	77.557
1.33 MPa	165.435	117.913	47.522	152.593	74.324	78.269
	158.971	128.017	30.954	155.784	72.461	83.323
	165.704	120.846	44.858	152.133	72.334	79.799
1.43 MPa	155.151	130.06	25.091	158.008	74.582	83.426
	162.611	134.514	28.097	152.489	84.746	67.743

	153.821	137.116	16.705	150.817	78.976	71.841
1.67 MPa	165.215	139.555	25.660	154.356	80.772	73.584
	159.389	126.969	32.420	150.099	76.386	73.713
	169.421	129.509	39.912	152.643	80.977	71.666
2.00 MPa	158.937	127.297	31.640	152.007	99.857	52.150
	163.082	132.244	30.838	146.156	74.489	71.667
	171.709	137.241	34.468	149.945	43.828	76.117
2.22 MPa	153.200	137.528	15.672	160.628	82.619	78.009
	166.565	126.696	39.869	153.278	95.115	58.163
	161.714	141.231	20.483	147.45	83.278	64.172
2.86 MPa	165.124	131.604	33.520	161.198	71.085	90.113
	163.253	131.143	32.110	159.300	82.218	77.082
	165.662	132.949	32.713	143.948	78.900	65.048

Table 5. Advancing and receding angle data for 50W 25L 100H (µm) and 50W 50L 100H (µm)

	50W 25L 100H (µm)			***50W 50L 100H (µm)***		
	Adv. Angle (º)	Rec. Angle (º)	Hysteresis (º)	Adv. Angle (º)	Rec. Angle (º)	Hysteresis (º)
1.18 MPa	157.308	99.308	57.825	167.412	100.973	66.439
	155.347	90.808	64.539	166.152	105.998	60.154
	158.455	88.730	69.725	164.928	104.255	60.673

1.33 MPa	167.500	97.331	70.169	163.769	113.156	50.613
	157.559	96.011	61.548	166.152	121.297	44.855
	159.775	93.687	66.088	160.730	105.513	55.217
1.43 MPa	152.295	95.567	56.728	160.432	108.624	51.808
	152.754	95.172	57.582	150.247	105.544	44.703
	157.685	97.966	59.719	159.560	106.671	52.889
1.67 MPa	152.637	101.783	50.854	152.005	110.363	41.642
	157.107	98.379	58.728	161.831	115.408	46.423
	158.515	96.112	62.403	160.885	117.901	42.984
2.00 MPa	152.011	119.161	32.850	158.836	111.418	47.418
	162.156	91.274	70.882	155.423	108.408	47.015
	152.913	92.803	60.110	155.094	118.924	36.170
2.22 MPa	160.105	113.067	47.038	160.288	115.530	44.758
	153.111	106.528	46.583	163.524	109.430	54.094
	164.773	106.508	58.265	158.547	106.172	52.375
2.86 MPa	155.351	95.518	59.833	158.512	108.932	49.580
	149.168	94.880	54.288	164.132	120.021	44.111
	154.011	98.723	55.288	164.972	115.126	49.846

Appendix C

Nomenclature

Table 6. Variable nomenclature

Symbol	***Definition***
γ_{SV}	Surface energy at the solid-vapor interface
γ_{SL}	Surface energy at the solid-liquid interface
γ_{LV}	Surface energy at the liquid-vapor interface
θ	Contact angle on a smooth surface
θ^*	Predicted apparent angle of a Cassie-state droplet
f_1	Fraction of solid on a surface
f_2	Fraction of air on a surface
r	Roughness factor
w	Micropillar width
h	Micropillar height
l	Spacing between micropillars
θ_W	Predicted apparent angle of a Wenzel-state droplet
Φ_{sf}	Solid fraction

r_c	Critical roughness to transition between Cassie state and Wenzel state
m	Droplet mass
w_d	Droplet width
g	Gravitational acceleration
σ	Surface tension
θ_{adv}	Advancing angle
θ_{rec}	Receding angle
θ_{slide}	Sliding angle
V_s	Critical drop volume for spreading on a hairy surface
β	Geometry-dependent constant used to determine critical drop volume for spreading on hairy surfaces
r_d	Radius of droplet
d_0	Diameter of the bottom of a hair
d_s	Diameter at point of contact with droplet
L	Hair length
B	Bending stiffness
E_{el}	Energy absorbed in bending flexible hairs
E	Young's modulus
R	Hair radius

h	Height at which hair contacts a droplet
u	Deflection at height h on a hair
E_{wet}	Wetting energy of a droplet
θ_{cyl}	Contact angle at a fluid interface with hair
q	Inverse capillary length
ρ	Water density
n	Ratio of PDMS curing agent to base
δ_x	Horizontal end-point deflection of cantilever beam
F	Applied end-point cantilever beam force
I	Area moment of inertia

BIBLIOGRAPHY

[1] Mekonnen, Mesfin M., and Arjen Y. Hoekstra. "Four billion people facing severe water scarcity." *Science advances* 2, no. 2 (2016): e1500323.

[2 Koch, Kerstin, Bharat Bhushan, and Wilhelm Barthlott. "Diversity of structure, morphology and wetting of plant surfaces." *Soft Matter* 4, no. 10 (2008): 1943-1963.

[3] Brewer, C. A., W. K. Smith, and T. C. Vogelmann. "Functional interaction between leaf trichomes, leaf wettability and the optical properties of water droplets." *Plant, Cell & Environment*14, no. 9 (1991): 955-962.

[4] Neinhuis, C., and W. Barthlott. "Characterization and distribution of water-repellent, self-cleaning plant surfaces." *Annals of botany* 79, no. 6 (1997): 667-677.

[5] Young, Thomas. "III. An essay on the cohesion of fluids." *Philosophical transactions of the royal society of London* 95 (1805): 65-87.

[6] Dufour, Renaud, Maxime Harnois, Yannick Coffinier, Vincent Thomy, Rabah Boukherroub, and Vincent Senez. "Engineering sticky superomniphobic surfaces on transparent and flexible PDMS substrate." *Langmuir* 26, no. 22 (2010): 17242-17247.

[7] Cassie, A. B. D., and S. Baxter. "Wettability of porous surfaces." *Transactions of the Faraday society* 40 (1944): 546-551.

[8] Wenzel, Robert N. "Resistance of solid surfaces to wetting by water." *Industrial & Engineering Chemistry* 28, no. 8 (1936): 988-994.

[9] Bico, José, Uwe Thiele, and David Quéré. "Wetting of textured surfaces." *Colloids and Surfaces A: Physicochemical and Engineering Aspects* 206, no. 1-3 (2002): 41-46.

[10] Furmidge, C. G. L. "Studies at phase interfaces. I. The sliding of liquid drops on solid surfaces and a theory for spray retention." *Journal of colloid science* 17, no. 4 (1962): 309-324.

[11] Yeh, Kuan-Yu, Li-Jen Chen, and Jeng-Yang Chang. "Contact angle hysteresis on regular pillar-like hydrophobic surfaces." *Langmuir* 24, no. 1 (2008): 245-251.

[12] Duprat, C., S. Protiere, A. Y. Beebe, and H. A. Stone. "Wetting of flexible fibre arrays." *Nature* 482, no. 7386 (2012): 510.

[13] Bernardino, Nelson Rei, Valentin Blickle, and Siegfried Dietrich. "Wetting of surfaces covered by elastic hairs." *Langmuir* 26, no. 10 (2010): 7233-7241.

[14] Wang, Zhixin, Alex A. Volinsky, and Nathan D. Gallant. "Crosslinking effect on polydimethylsiloxane elastic modulus measured by custom-built compression instrument." *Journal of Applied Polymer Science* 131, no. 22 (2014).

Academic Vita of Hannah Feldstein

hlf13@psu.edu

The Pennsylvania State University
Mechanical Engineering
Schreyer Honors College

Thesis Title: Effect of Elasticity on Liquid Repellency of Cassie-State Droplets on Superhydrophobic Surfaces
Thesis Supervisor: Professor Tak-Sing Wong

Research Experience

- Penn State Wong Laboratory for Nature Inspired Engineering, under supervision of Prof. Tak-Sing Wong, January 2016 – present
- Bio-Inspired Robotics REU at the University of Maryland, College Park, in Prof. Sarah Bergbreiter's Microrobotics Laboratory, Summer 2018
- Summer research in Wong Laboratory for Nature Inspired Engineering funded by PPG Industries, Summer 2016
- Internship at Penn State Engineering Design and Optimization Group, Summer 2014 (Senior in High School), under the supervision of Prof. Mary Frecker

Publications

- Stogin, B.B., L. Gockowski, **H. Feldstein**, H. Claure, J. Wang, and T.S. Wong, Free-standing liquid membranes as unusual particle separators. *Science Advances*. DOI: 10.1126/sciadv.aat3276 (2018).
    - Featured in Science: This Improbable Membrane Can Trap Flies in a Jar-and Odor in a Toilet, *Science*, doi:10.1126/science.aav2109, 24 August 2018
    - Selected Media Coverage:
        - Reverse filter is next big thing in surgery, The Times, August 25 2018
        - Une passoire inverse bloque les odeurs et les particules, Le Monde, September 4 2018
- Bowen, L., K. Springsteen, **H. Feldstein**, M. Frecker, T. W. Simpson, and P. von Lockette, Development and validation of a dynamic model of magneto-active elastomer actuation of the waterbomb base. *Journal of Mechanisms and Robotics*. doi:10.1115/1.4029290 (2015).

Presentations

- Poster at Penn State College of Engineering Research Initiative Symposium, *Passive Actuation of Elastic Slippery Rough Surfaces for Fog Harvesting*, April 18, 2018
- Invited Speaker in Mechanical Engineering Freshman Seminar, Topic: Research opportunities at Penn State, February 22, 2017

- PPG Summer Fellowship Presentation at Penn State University, *Characterization of Slippery Rough Surfaces: Drop Bouncing, Evaporation, and Self-Cleaning*, August 4, 2016
- PPG Summer Fellowship Presentation at PPG Industries in Pittsburg, *Characterization of Slippery Rough Surfaces: Drop Bouncing, Evaporation, and Self-Cleaning*, August 2, 2016
- PPG Summer Fellowship Poster Session at Penn State University, *Characterization of Slippery Rough Surfaces: Drop Bouncing, Evaporation, and Self-Cleaning*, July 20, 2016
- Design Poster at Penn State Design Showcase and Industry Partners' Reception (opportunity given to first place design team in engineering class), April 28, 2016
- Attended NSF Poster Session: 2015 Emerging Researchers National Conference in STEM, Washington DC, February 19-21, 2015 (Senior in High School)

Leadership/Teaching Experience

- Women in Engineering Program Facilitated Study Group Leader for Calculus of Several Variables (Math 231), January 2018 – present

Fellowships and Awards

- Women in Engineering Program Facilitated Study Group Scholarship, January 2018 - present
- College of Engineering Research Initiative REU Scholarship, Spring 2018
- Evan Pugh Senior Award, April 15 2018
- The President's Sparks Award, April 2 2017
- Tau Beta Pi, The Engineering Honors Society, Spring 2017
- The President's Freshman Award, April 3 2016
- PPG Undergraduate Research Fellowship, Summer 2016
- Schreyer Honors College Academic Excellence Scholarship, awarded per semester, Fall 2015 - present
- 1st Place Award REM (Research Experience and Mentoring) Poster Session at 2015 Emerging Researchers National Conference in STEM, Washington, DC, February 19-21, 2015